

Multi-phase field approach to tensile fracture and compressive crushing in grained heterogeneous materials

Pietro Lenarda^{a,*}, José Reinoso^b and Marco Paggi^a

^aIMT School for Advanced Studies Lucca, Piazza S. Francesco 19, Lucca, 55100, Italy

^bElasticity and Strength of Materials Group, School of Engineering, Universidad de Sevilla, Camino de los Descubrimientos s/n, Seville, 41092, Spain

ARTICLE INFO

Keywords:

Phase field approach to fracture

Crushing damage

Finite element method

Coupled problem

Mesoscale model of concrete

Abstract

The variational approach to brittle fracture is herein extended to deal with the simultaneous interplay of two failure mechanisms affecting grained heterogeneous materials in compression, namely fracture in tension and crushing in compression. The problem is addressed in the context of a multi-phase field variational approach, with two independent damage variables associated to each failure mechanism. The proposed computational method implemented in the open source FEniCS finite element software is applied to 2D mesoscale models of concrete specimens in compression. The predicted trends for specimens with different aspect ratios and different degree of lateral confinement are consistent with experimental trends on apparent compressive strength and with typically observed failure patterns.

Nomenclature

E_m	Young's modulus of the matrix [MPa]
E_a	Young's modulus of aggregates [MPa]
ν_m	Poisson's ratio of the matrix
ν_a	Poisson's ratio of aggregates
$G_{c,m}$	Fracture energy of the matrix [N/mm]
$G_{c,a}$	Fracture energy of the aggregates [N/mm]
$G_{c,cm}$	Crushing energy of the matrix [N/mm]
$G_{c,ca}$	Crushing energy of the aggregates [N/mm]
$l_{c,m}$	Internal length-scale of the matrix [mm]
$l_{c,a}$	Internal length-scale of the aggregates [mm]
$l_{c,cm}$	Internal length-scale of the matrix in compression [mm]
$l_{c,ca}$	Internal length-scale of the aggregates in compression [mm]
R_c	Cubic compressive strength [MPa]
f_c	Cylindrical compressive strength [MPa]

1. Introduction

Multi-field variational formulations (usually denominated phase field methods in the literature) have attracted a significant attention by the research community as a versatile tool for fracture mechanics simulations. Such an approach accounts for a nonlocal phase variable governed by a Poisson-type partial differential equation to model fracture events, see [1, 2]. Phase field shares some mathematical and modeling aspects with continuum damage mechanics [3, 4, 5, 6]. The foundations of phase field approaches for brittle fracture can be traced back to the classical energy-based Griffith criterion [7] through the introduction of a total energy functional that rules the competition between the elastic energy contribution and the dissipated fracture energy to create a new surface. The minimization of this functional allows triggering crack nucleation, propagation and coalescence in the continuum. Quasi-static phase field formulations for brittle fracture have been proposed by Bourdin et al. [8, 9] and the thermodynamically consistent framework has been extensively developed by Miehe et al.

*Corresponding author

✉ pietro.lenarda@imtlucca.it (P. Lenarda)
ORCID(s):

[10, 11] and by many authors afterwards [12, 13, 14, 15, 16, 17, 18, 19, 20, 21, 22, 23].

The basic method considers a decomposition of the strain energy density to degrade the elastic properties only in tension and not in compression. Various forms of decompositions have been proposed in the literature, including the deviatoric/volumetric splitting in [2], the model presented in [24], and the hybrid model [17].

However, brittle materials in compression exhibit a specific type of failure which involves material crushing, which is a mechanism of energy dissipation physically distinct from tensile fracture and, as such, it cannot be simulated within the existing phase field models. Experimental uniaxial compressive tests on concrete specimens [25, 26, 27] highlight the occurrence of a mechanisms of material crushing which leads to a specific energy dissipation in compression which is one order of magnitude higher than in tension. Moreover, they show the existence of an internal length scale corresponding to the band where energy dissipation takes place. Based on those considerations, the *overlapping crack model* for damage in compression was pioneeringly proposed by Carpinteri et al. [28], in close analogy with the *cohesive zone model* in tension. The idea was to model the effect of diffused energy dissipation during crushing events as an equivalent single crack in compression where the energy dissipated is the result of the work done by compressive tractions multiplied by a fictitious material compenetration.

Although successfully applied to concrete specimens in compression [29, 30] and to beams in three-point bending [31] with a single tensile/overlapping crack, there is indeed the need of an energetically rigorous fracture mechanics model that could be applied not only at the global scale, but also at the mesoscale.

Here, following the above seminal concepts, a novel multi-phase field model for fracture in tension and crushing in compression is proposed. The fundamental idea is to distinguish the two damage mechanisms and related energy dissipations in tension and compression, associating two independent phase field variables. Moreover, while the phase field variable for fracture will degrade the strain energy density associated to a tensile stress state, with its specific fracture energy and internal length scale, the additional phase field damage for crushing will be used to degrade the strain energy density associated to the compressive stress state, with also its associated crushing energy and internal length scale. Both phase field variable evolutions will be ruled by a Poisson-type partial differential equation, as done in single phase field models.

The methodology is herein employed to simulate complex damage patterns observed in compressive tests of concrete specimens at the mesoscale with different aspect ratios and with different degree of lateral confinement [32, 33]. Experimental results show that slender cylindrical specimens usually fail due to splitting failure modes, due to the propagation of sub-vertical cracks parallel to the loading direction. On the other hand, cubic specimens tend to fail due to diagonal crack propagation, while even shorter specimens show a failure mode dominated by fragmentation. With the aim of the proposed model, it will be shown that a full range of damage patterns can be simulated in 2D mesoscale models of concrete specimens, generated with a statistical distribution of aggregates with diameters obeying the Füller distribution density function proposed in [34].

2. Mathematical formulation

Let consider an arbitrary body $\Omega \in \mathbb{R}^{n_{dim}}$ in the Euclidean space of dimension n_{dim} , in which an evolving internal discontinuity Γ is postulated. Here it is assumed that $\Gamma = \Gamma_f \cup \Gamma_c$, where Γ_f is associated to fracture caused by a tensile stress state, while Γ_c is associated to crushing caused by a compressive stress state. The position of a material point is denoted by the vector \mathbf{x} in the global Cartesian frame within the bulk. The body forces are denoted by $\mathbf{b} : \Omega \rightarrow \mathbb{R}^{n_{dim}}$. The boundary of the body is denoted by $\partial\Omega \in \mathbb{R}^{n_{dim}-1}$. Kinematic and traction boundary conditions are prescribed along the disjoining parts $\partial\Omega_u \subset \partial\Omega$ and $\partial\Omega_t \subset \partial\Omega$, respectively, with $\partial\Omega_t \cup \partial\Omega_u = \partial\Omega$ and $\partial\Omega_t \cap \partial\Omega_u = \emptyset$, yielding:

$$\mathbf{u} = \bar{\mathbf{u}} \text{ on } \partial\Omega_u \text{ and } \boldsymbol{\sigma} \cdot \mathbf{n} = \bar{\mathbf{T}} \text{ on } \partial\Omega_t, \quad (1)$$

where \mathbf{n} denotes the outward normal unit vector to the body, and $\boldsymbol{\sigma}$ is the Cauchy stress tensor.

The variational approach to brittle fracture and material crushing is set up through the definition of the following free energy functional:

$$\begin{aligned} \Pi(\mathbf{u}, \Gamma) &= \Pi_\Omega(\mathbf{u}, \Gamma) + \Pi_\Gamma(\Gamma) = \\ &= \int_{\Omega \setminus \Gamma} \psi^e(\boldsymbol{\varepsilon}) \, d\mathbf{x} + \int_{\Gamma_f} \mathcal{G}_c \, d\Gamma + \int_{\Gamma_c} \mathcal{G}_{c,c} \, d\Gamma, \end{aligned} \quad (2)$$

where $\psi^e(\boldsymbol{\varepsilon})$ is the elastic energy density that depends upon the strain field $\boldsymbol{\varepsilon}$, and $\mathcal{G}_c, \mathcal{G}_{c,c}$ are, respectively, the fracture energy in tension and the crushing energy in compression.

In many porous or grained materials, the fracture mode is induced by the combination of both tensile and compressive internal stress states. These micro-structurally complex materials exhibit very different fracture mechanisms in tension and compression. In general, the crushing energy can be one or two orders of magnitude greater than the fracture energy,

and plays a major role in the evolution of damage. The need for distinguish between more than one failure mechanism has been already claimed by many authors [36, 37], especially in concrete [5]. To account for these different damage mechanisms, a multi-phase field state vector $\mathbf{s} = (s_1, s_2)^T$ with two damage variable components is herein introduced, such that s_1 and s_2 are damage associated to tensile and compressive internal stress states, respectively.

In Eq.(2), the term $\Pi_\Omega(\mathbf{u}, \Gamma)$ identifies the elastic energy stored in the damaged body, while the energy required to create the crack complying with the Griffith criterion or a crushing zone is denoted by $\Pi_\Gamma(\Gamma)$. The dissipated energy in the bulk is a state function of the displacement \mathbf{u} and of the internal damage-like variables s_i , $i = 1, 2$, ($s_i \in [0, 1]$ $i = 1, 2$, where $s_i = 0$ represents an intact material, while $s_i = 1$ identifies the fully damaged state).

To account for different damage mechanisms, the following decomposition of the energy density is proposed:

$$\psi^e(\boldsymbol{\varepsilon}, s_1, s_2) = \{(1-s_1)^2 + k\} \psi_+^e(\boldsymbol{\varepsilon}) + \{(1-s_2)^2 + k\} \psi_-^e(\boldsymbol{\varepsilon}), \quad (3)$$

where the positive and negative parts of the energy density are defined as:

$$\psi_\pm^e(\boldsymbol{\varepsilon}) = \frac{\lambda}{2} \langle \text{Tr}(\boldsymbol{\varepsilon}) \rangle_\pm^2 + \mu \text{Tr}(\boldsymbol{\varepsilon}_\pm^2) \quad (4)$$

and λ and μ are the Lamé constants, $\text{Tr}(\cdot)$ denotes the trace operator, k is a parameter that defines a residual stiffness to prevent numerical instabilities in the computational implementation, and simultaneously preventing that the resulting system of equations becomes ill-conditioned. With reference to the spectral representation for the strain (with eigenvalues

ϵ_i and unit eigenvectors e_i), denoted as

$$\epsilon = \sum_{i=1}^3 \epsilon_i e_i \otimes e_i, \quad (5)$$

the strain is additively decomposed as $\epsilon = \epsilon_+ + \epsilon_-$, so that the tensile and compressive parts associated to ϵ are

$$\epsilon_{\pm} = \sum_{i=1}^3 \langle \epsilon_i \rangle_{\pm} e_i \otimes e_i, \quad (6)$$

respectively, where the Macaulay bracket operator is defined for every scalar x as $\langle x \rangle_{\pm} = (x \pm |x|)/2$.

Within the regularized framework of the phase field approach and in analogy with the formulation in tension [41, 42], a crushing density functional γ_c is herein introduced in addition to the crack density functional γ , to smear out damage not only in tension but also in compression:

$$\begin{aligned} \Pi(\mathbf{u}, s_1, s_2) = & \int_{\Omega} \psi^e(\epsilon, s_1, s_2) \, d\mathbf{x} + \int_{\Omega} G_c \gamma(s_1, \nabla s_1) \, d\mathbf{x} + \\ & + \int_{\Omega} G_{c,c} \gamma_c(s_2, \nabla s_2) \, d\mathbf{x}, \end{aligned} \quad (7)$$

where ψ^e is defined in Eq. (3). Here, $\nabla(\cdot)$ denoting the spatial gradient operator.

According to [10], the functional $\gamma(s_1, \nabla s_1)$ is set as a convex function composed by a quadratic term of the phase field variable s_1 and another quadratic term involving its gradient:

$$\gamma(s_1, \nabla s_1) = \frac{1}{2l} s_1^2 + \frac{l}{2} |\nabla s_1|^2, \quad (8)$$

where l is the internal length scale associated to brittle fracture. Similarly, we introduce here a functional $\gamma_c(s_2, \nabla s_2)$ to regularize the localized damage in compression caused by material crushing, this time function of the phase field

variable s_2 :

$$\gamma_c(s_2, \nabla s_2) = \frac{1}{2l_c} s_2^2 + \frac{l_c}{2} |\nabla s_2|^2, \quad (9)$$

where again another regularization length scale l_c is introduced, which in the most general case can be different from l .

The stress tensor corresponding to a generic state of damage is now given by:

$$\begin{aligned} \sigma = & \{ (1 - s_1)^2 + k \} (\lambda \langle \text{Tr}(\epsilon) \rangle_+ \mathbf{I} + 2\mu \epsilon_+) + \\ & + \{ (1 - s_2)^2 + k \} (\lambda \langle \text{Tr}(\epsilon) \rangle_- \mathbf{I} + 2\mu \epsilon_-) \end{aligned} \quad (10)$$

where \mathbf{I} denotes the second-order identity tensor. The thermodynamic consistency of the above constitutive theory, in agreement with the Clausius-Duhem inequality, can be proved in analogy with the procedure in [10].

3. Weak form and finite element formulation

In this section, the weak form corresponding to the multi-phase field model for brittle fracture and compressive crushing is derived and the corresponding finite element formulation is discussed. Let be respectively $\mathbf{H}^1(\Omega)$ and $H^1(\Omega)$ the vector and scalar spaces of square-integrable functions defined on Ω having first weak derivative which is square-integrable. And let be $\mathbf{H}_0^1(\Omega)$ and $H_0^1(\Omega)$ the corresponding functional spaces of vanishing functions on the boundary $\partial\Omega$. Following a standard Galerkin procedure, the weak form of the coupled displacement and fracture problem according

to Eq.(7) reads:

$$\begin{aligned} \delta\Pi(\mathbf{u}, s_1, s_2) = & \int_{\Omega} \boldsymbol{\sigma}(\mathbf{u}, s_1, s_2) : \boldsymbol{\varepsilon}(\mathbf{v}) \, d\mathbf{x} + \\ & - \int_{\Omega} 2P_1 H(1 - s_1)\phi_1 \, d\mathbf{x} + \\ & + \int_{\Omega} G_c \left\{ \frac{1}{l} s_1 \phi_1 + l \nabla s_1 \cdot \nabla \phi_1 \, d\mathbf{x} \right\} \\ & - \int_{\Omega} 2P_2 H_c(1 - s_2)\phi_2 \, d\mathbf{x} + \\ & + \int_{\Omega} G_{c,c} \left\{ \frac{1}{l_c} s_2 \phi_2 + l_c \nabla s_2 \cdot \nabla \phi_2 \, d\mathbf{x} \right\} - \delta\Pi_{\text{ext}}, \end{aligned} \quad (11)$$

where \mathbf{v} is the vector of virtual displacement defined on $\mathbf{H}_0^1(\Omega)$, ϕ_1, ϕ_2 stand for the phase field test functions defined on $H_0^1(\Omega)$, H and H_c are the strain history functions accounting for the irreversibility of the crack [10, 18, 39] and are defined as:

$$H = \max_{\tau \in [0, t]} \left\{ \{(1 - s_1)^2 + k\} \psi_+(\boldsymbol{\varepsilon}(\tau)) \right\}, \quad (12)$$

and

$$H_c = \max_{\tau \in [0, t]} \left\{ \{(1 - s_2)^2 + k\} \psi_-(\boldsymbol{\varepsilon}(\tau)) \right\} \quad (13)$$

where P_i are activation flags for current crack driving forces H and H_c [40] such that:

$$P_1 = \begin{cases} 1 & \text{if } \text{Tr}(\boldsymbol{\sigma}) > 0 \\ 0 & \text{otherwise} \end{cases} \quad \text{and} \quad P_2 = 1 - P_1. \quad (14)$$

Notice that the criterion adopted to activate the phase field evolution s_1 or s_2 is based on the computation of the internal state of stress in terms of the first invariant of the stress tensor $\text{Tr}(\boldsymbol{\sigma})$ which can be tensile or compressive [5]. It is worth noting that the present model is applicable only for monotonic loading conditions and should be extended to deal with cyclic loading. In a more complex scenario

involving a cyclic tensile/compressive loading, if an internal crack surface is created due to the tensile stress state in the bulk ($s_1 = 1$), then, in the case of load reversal caused by a subsequent compressive loading, a frictional contact model should be considered to describe the response of the crack flanks in contact. Without explicitly modelling the displacement discontinuity, which would introduce complexities that would highly reduce the advantages of a smeared damage formulation, a strategy could be based on the introduction of an internal history variable to track where damage reaches 1 in tension ($s_1 = 1$, i.e., a tensile crack is formed). Then, the constitutive model in the bulk should be modified, introducing effective elastic parameters that could take into account, in an effective way, the response of the embedded discontinuity subject to frictional contact.

Eq.(11) holds for any test functions \mathbf{v} and ϕ_1, ϕ_2 . The external contribution to the variation of the bulk functional in Eq.(11) is defined as follows:

$$\delta\Pi_{\text{ext}}(\mathbf{u}, \mathbf{v}) = \int_{\partial\Omega} \bar{\mathbf{T}} \cdot \mathbf{v} \, d\Gamma + \int_{\Omega} \mathbf{b} \cdot \mathbf{v} \, d\mathbf{x}. \quad (15)$$

For the finite element formulation, the mechanical problem reads: given the prescribed loading condition $\bar{\mathbf{u}}^n$ and traction $\bar{\mathbf{T}}^n$ at step n , find $\mathbf{u} \in \mathbf{U} = \{\mathbf{u} \mid \mathbf{u} = \bar{\mathbf{u}}^n \text{ on } \partial\Omega_u, \mathbf{u} \in \mathbf{H}^1(\Omega)\}$ such that:

$$\begin{aligned} \mathcal{E}_{\mathbf{u}}(\mathbf{u}, s_1, s_2; \mathbf{v}) = & \int_{\Omega} \boldsymbol{\sigma}(\mathbf{u}, s_1, s_2) : \boldsymbol{\varepsilon}(\mathbf{v}) \, d\mathbf{x} - \int_{\partial\Omega} \bar{\mathbf{T}}^n \cdot \mathbf{v} \, d\Gamma \\ & - \int_{\Omega} \mathbf{b} \cdot \mathbf{v} \, d\mathbf{x} = 0, \quad \forall \mathbf{v} \in \mathbf{H}_0^1(\Omega), \end{aligned} \quad (16)$$

while the two phase field problems are formulated as follows:

Find $s_1 \in H^1(\Omega)$ such that

$$\begin{aligned} \mathcal{E}_{s_1}(\mathbf{u}^k, s_1; \phi_1) &= \int_{\Omega} G_c l \nabla s_1 \cdot \nabla \phi_1 \, dx \\ &+ \int_{\Omega} \left\{ \frac{G_c}{l} + 2P_1 H \right\} s_1 \phi_1 \, dx \\ &- \int_{\Omega} 2P_1 H \phi_1 \, dx = 0, \quad \forall \phi_1 \in H_0^1(\Omega) \end{aligned} \quad (17)$$

and $s_2 \in H^1(\Omega)$ such that

$$\begin{aligned} \mathcal{E}_{s_2}(\mathbf{u}^k, s_2; \phi_2) &= \int_{\Omega} G_{c,c} l_c \nabla s_2 \cdot \nabla \phi_2 \, dx \\ &+ \int_{\Omega} \left\{ \frac{G_{c,c}}{l_c} + 2P_2 H_c \right\} s_2 \phi_2 \, dx \\ &- \int_{\Omega} 2P_2 H_c \phi_2 \, dx = 0, \quad \forall \phi_2 \in H_0^1(\Omega). \end{aligned} \quad (18)$$

To solve the quasi-static evolution problems for brittle fracture and compressive crushing, isoparametric linear triangular finite elements are used for the spatial discretization, and a staggered solution scheme is considered for the coupled problem. Staggered schemes based on alternate minimization exploit the convexity of the energy functional with respect to each individual variable \mathbf{u} and s_i , $i = 1, 2$ [10]. Here, an *ad hoc* developed solver has been implemented in the software FEniCS, see Alg. 1 for the algorithm description.

Algorithm 1 Staggered iterative scheme for multi-phase field fracture at a step $n \geq 1$

- 1: **Input:** Displacements and phase fields $(\mathbf{u}^{n-1}, s_1^{n-1}, s_2^{n-1})$ and prescribed loads $(\bar{\mathbf{u}}^n, \bar{\mathbf{T}}^n)$;
 - 2: Initialize $(\mathbf{u}_0, s_1^0, s_2^0) := (\mathbf{u}^{n-1}, s_1^{n-1}, s_2^{n-1})$;
 - 3: **for** $k \geq 1$ staggered iteration **do**;
 - 4: Given s_1^{k-1}, s_2^{k-1} , solve the mechanical problem:
 $\mathcal{E}_{\mathbf{u}}(\mathbf{u}, s_1^{k-1}, s_2^{k-1}; \mathbf{v}) = 0$ for \mathbf{u} , set $\mathbf{u} := \mathbf{u}^k$;
 - 5: Given \mathbf{u}^k , solve the phase field problems
 $\mathcal{E}_{s_i}(\mathbf{u}^k, s_i; \phi) = 0$ for s_i ($i = 1, 2$) and set $s_i := s_i^k$;
 - 6: **if** $\max\{ \|\mathbf{u}^k - \mathbf{u}^{k-1}\| / \|\mathbf{u}^{k-1}\|, |s_1^k - s_1^{k-1}| / |s_1^{k-1}|, |s_2^k - s_2^{k-1}| / |s_2^{k-1}| \} < \text{tol}$: **then**
 - 7: set $(\mathbf{u}^k, s_1^k, s_2^k) := (\mathbf{u}^n, s_1^n, s_2^n)$;
 - 8: **else** $k + 1 \rightarrow k$.
 - 9: **end if**
 - 10: **end for**
 - 11: **Output:** $(\mathbf{u}^n, s_1^n, s_2^n)$.
-

Despite the splitting of the two problems makes the phase field problem linear, the mechanical problem is still nonlinear because of the spectral decomposition of the strain tensor. In this work, the procedure based on the derivatives of the eigensystem is adopted to linearize the jacobian, based on the work in [20].

The linear form defined by the residual is given by:

$$\begin{aligned} F_{\mathbf{u}}(\mathbf{u}; \mathbf{v}) &= \int_{\Omega} ((1 - s_1)^2 + k) \sigma_+(\mathbf{u}) : \epsilon(\mathbf{v}) \, dx + \\ &+ \int_{\Omega} ((1 - s_2)^2 + k) \sigma_-(\mathbf{u}) : \epsilon(\mathbf{v}) \, dx + \\ &- \int_{\partial\Omega} \bar{\mathbf{T}} \cdot \mathbf{v} \, d\Gamma - \int_{\Omega} \mathbf{b} \cdot \mathbf{v} \, dx. \end{aligned} \quad (19)$$

Given \mathbf{u}^k the current Newton-Raphson approximate solution at iteration k , the correction $\delta\mathbf{u}$ is therefore the solution of the following linear variational problem: find $\delta\mathbf{u} \in \mathbf{U}_0 = \{ \mathbf{u} \mid \mathbf{u} = \mathbf{0} \text{ on } \partial\Omega_u, \mathbf{u} \in \mathbf{H}^1(\Omega) \}$ such that $J_{\mathbf{u}}(\delta\mathbf{u}, \mathbf{u}^k, s_1, s_2; \mathbf{v}) = -F_{\mathbf{u}}(\mathbf{u}^k, s_1, s_2; \mathbf{v})$, $\forall \mathbf{v} \in \mathbf{H}_0^1(\Omega)$, and then iterate as $\mathbf{u}^{k+1} = \mathbf{u}^k + \delta\mathbf{u}$. The Jacobian entering the formulation is

$$\begin{aligned} J_{\mathbf{u}}(\delta\mathbf{u}, \mathbf{u}; \mathbf{v}) &= \int_{\Omega} ((1 - s_1)^2 + k) \partial\sigma_+(\delta\mathbf{u}, \mathbf{u}) : \epsilon(\mathbf{v}) \, dx + \\ &+ \int_{\Omega} ((1 - s_2)^2 + k) \partial\sigma_-(\delta\mathbf{u}, \mathbf{u}) : \epsilon(\mathbf{v}) \, dx ; \end{aligned}$$

for details about the terms $\partial\sigma_-$, $\partial\sigma_+$ the reader is referred to [20].

The formulation has been implemented in the open source finite element software FEniCS [43].

4. Mesoscale model of concrete specimens with aggregates

The material mesostructure of concrete and other particulate materials is described by a Pareto distribution [34] of grain diameters d . In particular, let ϕ_{\min} and ϕ_{\max} denote the minimum and maximum grain size of a particulate material,

and defining the ratio $\alpha = \phi_{\max}/\phi_{\min}$, the probability density function of the diameter for the grain size in a volume is:

$$f_d(d) = \frac{\tau}{1 - \alpha^{-\tau}} \frac{\phi_{\min}^{\tau}}{d^{\tau+1}}, \quad (20)$$

where the exponent τ varies typically between 2 and 3.5. The value $\tau = 2$ corresponds to the distribution of perfect self-similarity. The case $\tau = 2.5$ is the so called Füller mix, which is the most common in concrete technology. To construct 2D surrogates of the 3D mesostructure, the probability density function $g_d(d)$ of the grain diameters intercepted by a plane is:

$$g_d(d) = \frac{\tau - 1}{1 - \alpha^{-(\tau-1)}} \frac{\phi_{\min}^{\tau-1}}{d^{\tau}}. \quad (21)$$

Under the assumption that the grains are circular, a series of randomly distributed locations of circles has been generated in Matlab according to the Füller mix. The coordinates and radii of the circles have been used to generate mesh samples to be tested in silico (virtual) compressive tests.

The present formulation could be extended to consider also an additional micro-scale of grains having diameter lower than ϕ_{\min} by using the probability density function in [44].

Considering $\phi_{\min} = 4$ and $\phi_{\max} = 16$, the order of magnitude of number of aggregates intercepted by a plane in a cubic specimen of 100 mm lateral size is 10^2 , which requires a fine finite element mesh to properly discretize the thin ligaments of mortar in between the particles. Correspondingly, the number of linear triangular finite elements required to discretize a cubic specimen is of the order of 10^4 . The computation time requested to solve a compressive test is of the order of 2 hours on a laptop ASUSPRO P3540FA-BQ1244R, Intel® Core™ i7, 1.8 GHz, 8 GB, 256 GB.

5. Effect of friction on the compressive strength of cubic and cylindrical samples

In this section, two geometries of a mesoscale concrete sample are considered, namely: a square of size $L = 100$ mm and a rectangle having a base of $L = 100$ mm and height $H = 200$ mm, which correspond to 2D replica of cubic and cylindrical specimens. For each of the two geometries, a number $N = 10$ of random mesostructure realizations are generated and tested. A plane stress state is assumed in all the cases.

The material properties of the aggregates (a) and the matrix (m) are, respectively, $E_a = 90$ [MPa], $E_m = 10$ [MPa], $\nu_a = 0.22$, $\nu_m = 0.33$, $G_{c,a} = 16$ [N/mm], $G_{c,m} = 0.016$ [N/mm], $l_a = 0.39$ [mm], $l_m = 0.0009$ [mm]. For crushing, we set $G_{c,c} = 1.5$ [N/mm] and $l_c = 0.0009$ [mm] for both aggregate and matrix.

The present model allows simulating a fracture process into the matrix or inside the aggregates. The crack path can pass along the interface between the two phases, but a specific constitutive response of the interfacial transition zone has not been set. Modelling the interfacial transition zone between aggregates and cement paste could be important, but especially for high strength concrete, where the crack path is strongly influenced by the high adhesion between the two material phases. In this case, an annulus of finite elements around the aggregates, with specific phase field parameters, could be introduced to distinguish their specific responses, inspired by [45]. Alternatively, interface finite elements with cohesive zone models could be inserted at the interface, as for fiber-reinforced composites [46].

In the simulations, a compressive displacement $\bar{u} = -5 \times 10^{-3}$ mm is imposed on the top side of the sample. Two set of boundary conditions are considered for the numerical simulations, namely low friction and high friction,

corresponding respectively to full slip and full slip regimes, see Fig. 1. Details of the finite element meshes used in the simulation are shown in Fig. 2. The mesh size is chosen as $h < \min \{l_m, l_c/2\}$. Low friction is simulated by imposing $u_y = 0$ on the lower boundary of the sample, which corresponds to a situation where lateral displacements are allowed as in the case of a vanishing friction coefficient between the specimen and the steel platen when a lubricant or Teflon is inserted. High friction is simulated by setting $u_x = u_y = 0$ on the specimen base, fully restraining the lateral displacements as it happens for a very high friction coefficient, see [33].

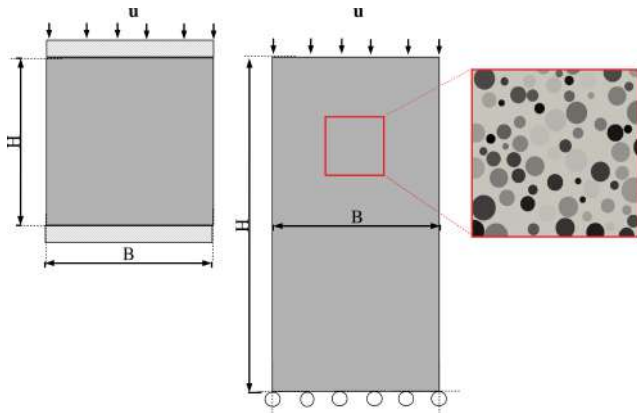


Figure 1: Schemes of the specimens for the numerical simulation: **a:** $H/B = 1$ cubic concrete sample under high friction boundary condition. **b:** $H/B = 2$ cylindrical concrete sample under low friction boundary conditions. **c:** Mesoscale structure corresponding to a Füller mix of grains used to generate the finite element meshes.

Figure 3(a) depicts the envelope (in grey color) of the whole set of predicted stress-displacement curves obtained from the numerical simulations for $H/B = 1$ (cubic specimen) and low friction boundary conditions. The average response over 10 random realizations of the mesostructure is shown with a solid curve in red. As a qualitative comparison with experimental data, although referring to a single compression test, we report with square dots the stress-displacement curve related to normal strength concrete specimens taken from [30], which has similar cubic

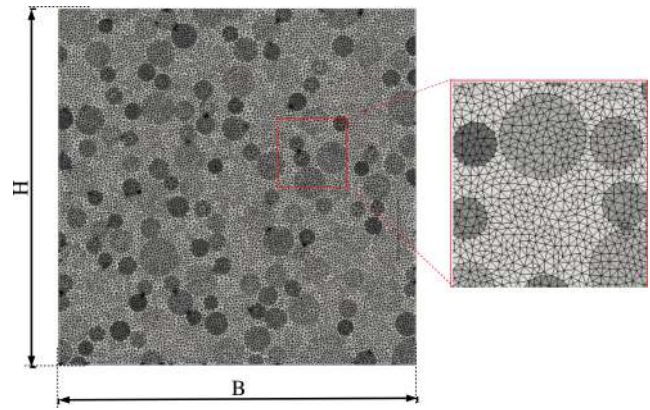


Figure 2: Typical finite element mesh used for the numerical simulation and detail of the mesoscale aggregate structure.

geometry and material properties as those herein used in the simulations. The experimental data are representative of the behaviour of a specimen without lateral confinement, i.e. the sample has been tested by interposing Teflon between the steel platen and concrete. Fig. 3(b) shows the same results but in the case of high friction boundary conditions.

The deformed mesh with the crack pattern and the corresponding contour plots of the phase field variable s_1 , associated to tensile fracture, and s_2 , associated to compressive crushing, is shown in Fig. 4 for three increasing values of the applied strain level. They refer to one representative simulation among the 10 tests on random realizations of the cubic specimen with low friction boundary conditions. Due to a lack of frictional restraint at the boundaries, portions of the specimen tend to separate from the sides by splitting, as highlighted by the vertical alignment of phase field cracks in the contour plot of s_1 . Crushing is almost absent, as highlighted by the contour plot of s_2 .

By changing the boundary conditions as high friction on the same specimen, the deformed mesh with the crack pattern and the corresponding contour plots of the phase field variables s_1 and s_2 significantly change, as shown in Fig. 5. The frictional restraint at the boundaries reduces the

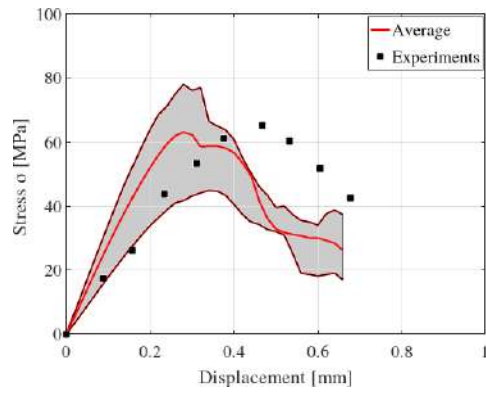
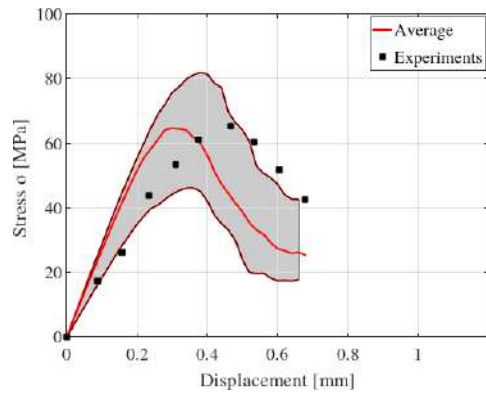

 (a) $H/B = 1$, low friction boundary conditions

 (b) $H/B = 1$, high friction boundary conditions

Figure 3: Numerical results on compressive tests on $H/B = 1$ cubic sample under low friction and high friction boundary conditions. The shaded areas represent the envelope of numerical predictions resulting from 10 random realizations of the material mesostructure. Experimental data on a specimen with the same geometry and similar material properties taken from [30] are reported for a qualitative comparison.

amount of sub-vertical splitting cracks, as highlighted in the contour plot of s_1 , while material crushing takes place diagonally, leading to a shear band formation, as shown in the contour plot of s_2 .

Figure 6(a) depicts the envelope (in grey color) of the whole set of predicted stress-displacement curves obtained from the numerical simulations for $H/B = 2$ (cylindrical specimen) and low friction boundary conditions. The average response over 10 random realizations of the mesostructure is shown with a curve in red. Figure 3(b) shows the same results but in the case of high friction boundary conditions. Again, as a qualitative comparison with experimental data, although referring to a single compression test, we report

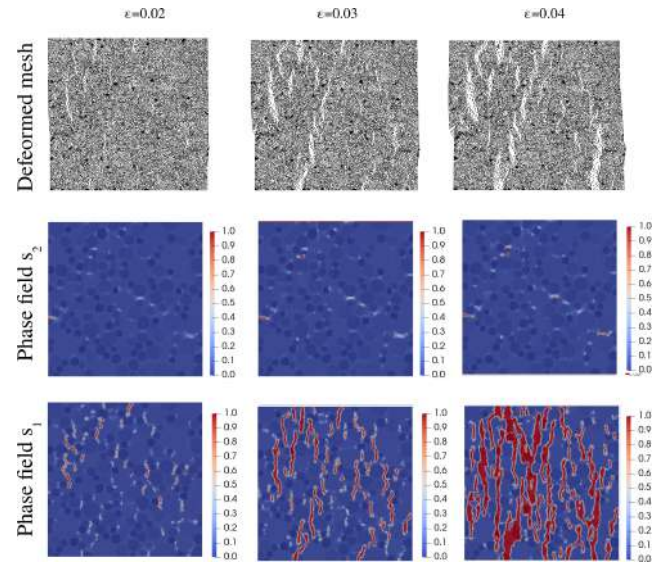


Figure 4: Crack pattern and phase field variables for a simulated compression test on a cubic specimen $H/B = 1$ under low friction conditions, for three applied strain levels.

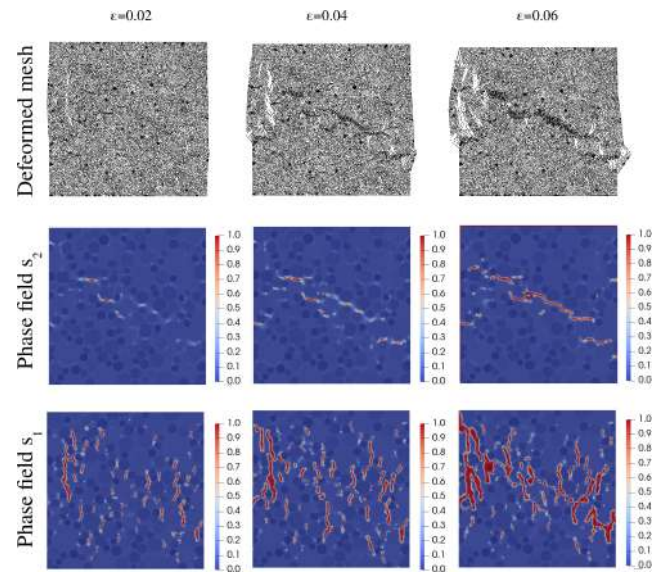


Figure 5: Crack pattern and phase field variables for a simulated compression test on a cubic specimen $H/B = 1$ under high friction conditions, for three applied strain levels.

with square dots the stress-displacement curve related to normal strength concrete specimens taken from [30], which has similar material properties and cylindrical geometry as those herein used in the simulations and have been tested without lateral confinement. The computational model is

able to predict the increased deformation of the post-peak branch at failure, as compared to cubic specimens.

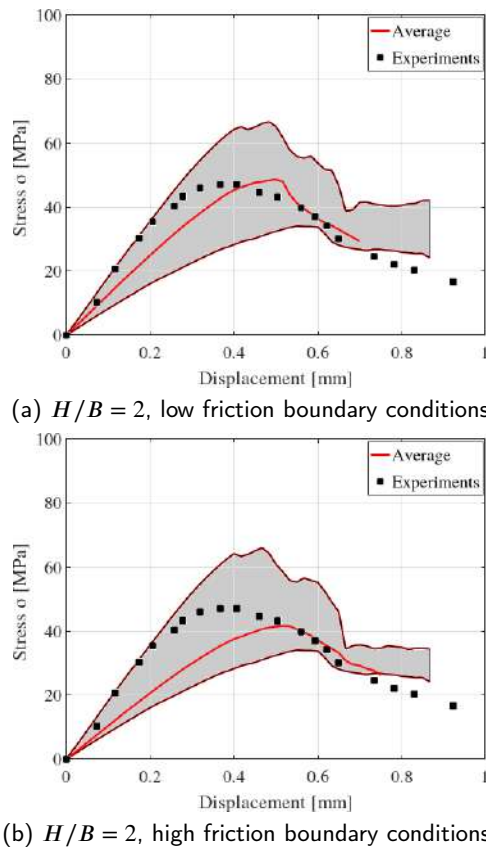


Figure 6: Numerical results on compressive tests on $H/B = 2$ cylindrical samples under low friction and high friction boundary conditions. The shaded areas represent the envelope of numerical predictions resulting from 10 random realizations of the material mesostructure. Experimental data on a specimen with the same geometry and similar material properties taken from [30] are reported for a qualitative comparison.

The deformed mesh with the crack pattern of one of the 10 tests on random realizations of the cylindrical specimen with low friction boundary conditions is shown in Fig.7, along with the contour plot of the phase field variables s_1 and s_2 . Failure is the result of subvertical tensile splitting cracks that are laterally unconfined due to the low friction boundary conditions.

The same results in case of high friction boundary conditions, depicted in Fig.8, show some crushing occurring in the middle portion of the specimen on the left side, which

originates a kind of internal hinge enhancing the formation of splitting cracks on the right side.

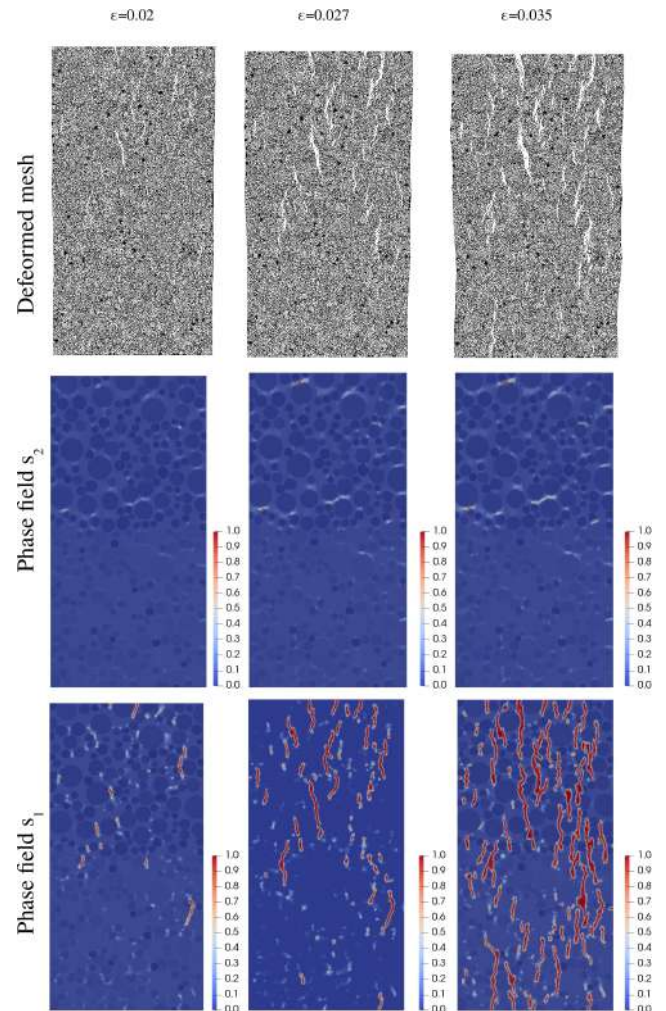


Figure 7: Crack pattern and phase field variables for a simulated compression test on a cylindrical specimen $H/B = 2$ under low friction conditions, for three applied strain levels.

In the former situation, the lateral deformation is enhanced due to the low friction coefficient, whereas in the latter the contact surface is in stick condition, i.e. with vanishing relative tangential displacements between platen and concrete along the interface. It can be noticed that the fracture patterns is very different in the case of extcolorbluehigh friction and extcolorbluelow friction boundary conditions. In the first case, it can be noticed the formation of shear bands and crushing in compression, while in the second case

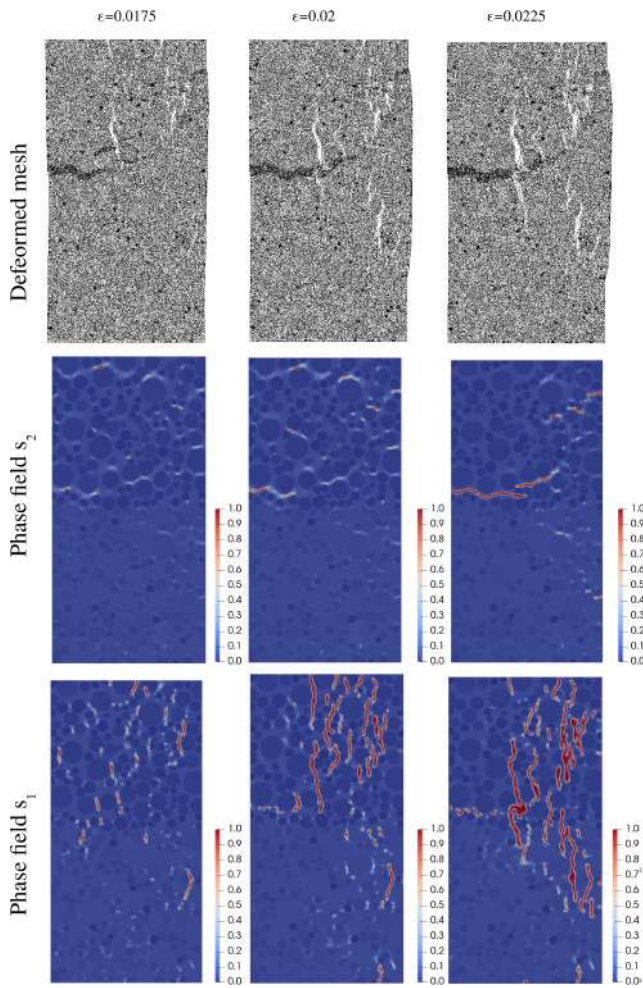


Figure 8: Crack pattern and phase field variables for a simulated compression test on a cylindrical specimen $H/B = 2$ under high friction conditions, for three applied strain levels.

the lateral expansion is allowed, thus inducing multiple crack patterns in the direction parallel to the imposed load related to internal states of tensile stress.

The randomness of the material mesostructure has an important effect on the scatter of the 2D numerical predictions. In order to provide a further quantitative comparison with experimental trends, to assess the predictive capabilities of the proposed computational method, we examine how the cubic and the cylindrical compressive strengths are affected by the frictional conditions applied to the boundary of the specimen. It is in fact well-known from experiments and simulations [33] that the cubic compressive strength, R_c , is

significantly affected by friction, while slender cylindrical specimens with aspect ratios $H/D > 2$ are minimizing such an effect upon the cylindrical compressive strength f_c .

To this aim, the set of force-displacement curves from numerical simulations is analyzed by extracting the compressive strengths R_c and f_c as the maximum values of the stress level reached during the test. Due to the randomness in the material mesostructure, we also associate to each simulated test a value of the equivalent Young's modulus in compression, E^* , computed as the slope of the stress-strain curve by linear interpolation within the strain level of $\varepsilon = 0.2\%$.

Numerical results are depicted in Fig.9 for (a) cubic and (b) cylindrical specimens. In each plot, in addition to the individual values extracted from each virtual experiment, we reported also the average strength values for the extcolorbluelow friction boundary condition (solid line) and for the extcolorbluehigh friction boundary condition (dashed line). Numerical results confirm the experimental trends. The average cubic compressive strength is significantly affected by friction between steel platens and the concrete specimen: the average value of R_c increased from 66.9 MPa (extcolorbluelow friction) up to 80.8 MPa (extcolorbluehigh friction), while the effect is almost negligible for cylindrical specimens where the average value f_c is 52.1 MPa (extcolorbluelow friction) or 54.4 MPa (extcolorbluehigh friction).

Moreover, again consistently with experimental trends [33], the cubic compressive strength is higher than the cylindrical compressive strength. The numerically predicted conversion ratio from cylinder to cubic strength, f_c/R_c , varies from 0.8 for extcolorbluelow friction boundary conditions to 0.6 in the case of extcolorbluehigh friction. Numerical predictions based on an elastoplastic model for concrete and frictional contact between the steel platen and concrete in

[33] predicted $f_c/R_c = 0.9$ for extcolorbluelow friction and $f_c/R_c = 0.78$ for a lateral confinement given by a friction coefficient of 0.6.

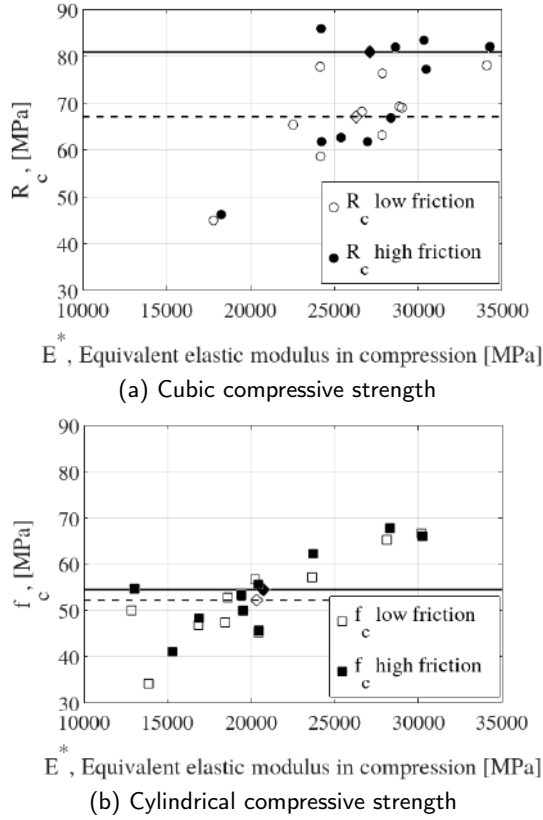


Figure 9: Predicted cubic, R_c , and cylindrical, f_c , compressive strengths vs. equivalent elastic modulus in compression, E^* . Dashed lines refer to high friction boundary conditions, while solid lines refer to low friction boundary conditions.

6. The role of the crushing energy and the interplay with tensile fracture

In this section, a rectangular sample with very small aspect ratio $H/B = 0.5$ is simulated, with base $B = 200$ mm, and height $H = 100$ mm, and it is subjected to a compressive test with low friction boundary conditions. This case study is chosen as representative of a situation where material crushing is often observed in the experiments [32].

The material parameters and the mesostructural features are the same as those considered in the previous section,

except for the crushing energy which is parametrically varied as $G_{c,c}/G_c = \{25, 50, 150, 200\}$, where G_c is the fracture energy. The stress/displacement curves obtained for numerical simulations of compressive tests are collected in Fig. 10.

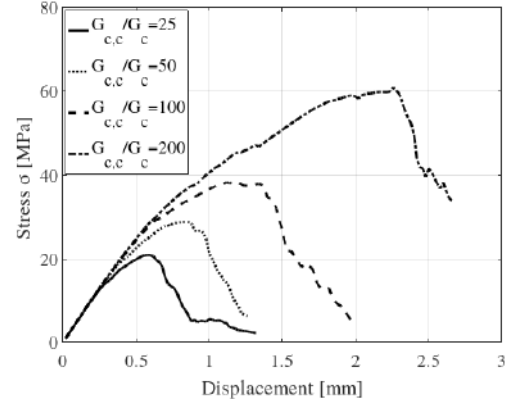


Figure 10: Stress vs. displacement curves from numerical simulations of compressive tests on a sample with $H/B = 0.5$, for different crushing energies.

By increasing $G_{c,c}$, the peak stress in the force-displacement curves largely increases. To explain the reasons behind such an effect, we compare in Figs. 11, 12 and 13 the crack pattern on the deformed mesh, the phase field variable s_1 associated to tensile fracture, and the phase field variable s_2 associated to crushing for the cases $G_{c,c}/G_c = 25$ and 200, as limit cases.

For $G_{c,c}/G_c = 25$, which implies a crushing energy 25 times higher than the fracture energy, both failure mechanisms occur under the form of a series of sub-vertical splitting cracks governed by the phase field variable $s_1 = 1$. Crushing also takes place, and it is activated for $\epsilon > 0.03$. Specifically, from the contour plot of s_2 , we note the formation of three initially separated sub-horizontal crushing zones that eventually coalesce at failure.

For $G_{c,c}/G_c = 200$, the energy to be dissipated due to crushing is 4 times higher than in the previous case study, and 100 times higher than the fracture energy. As a consequence, the competition between cracking and crushing is

favoring tensile crack propagation, since the corresponding failure mechanism requires less energy to dissipate in order to reach the condition $s_1 = 1$. The resulting crack pattern is close to that observed in the case of fragmentation.

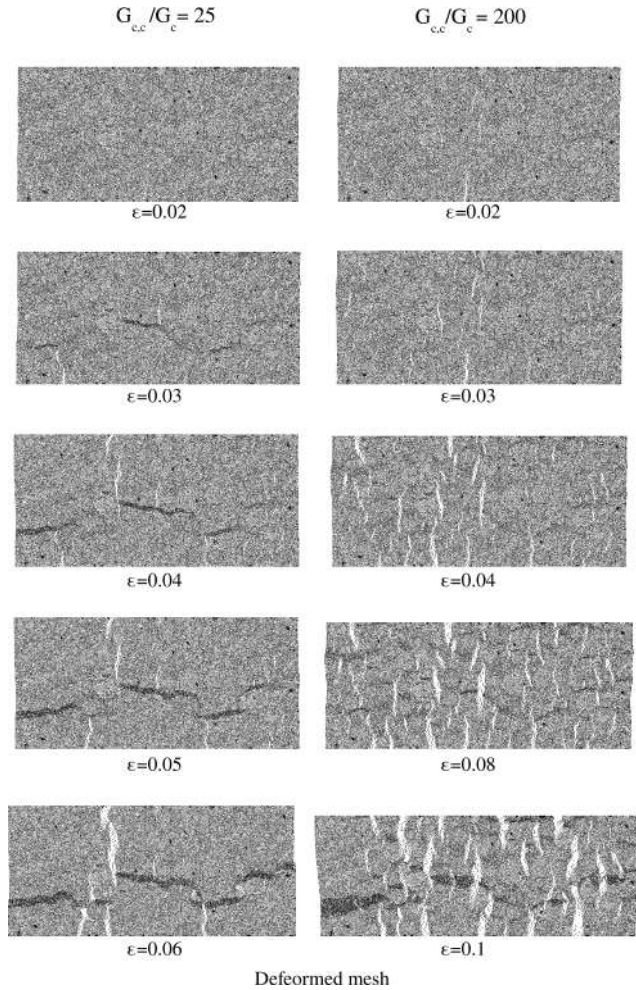


Figure 11: Deformed mesh of the sample with $H/B = 0.5$ and low friction conditions, for different strain levels of increasing value from the top to the bottom. On the left the case with $G_{c,c}/G_c = 25$, while on the right the case with $G_{c,c}/G_c = 200$.

7. Conclusion

In this work, a variational approach to brittle fracture in tension and compressive crushing in compression has been proposed through a multiple (two) phase field approach. The proposed methodology allows simulating the two different physical failure mechanisms associated to tensile fracture

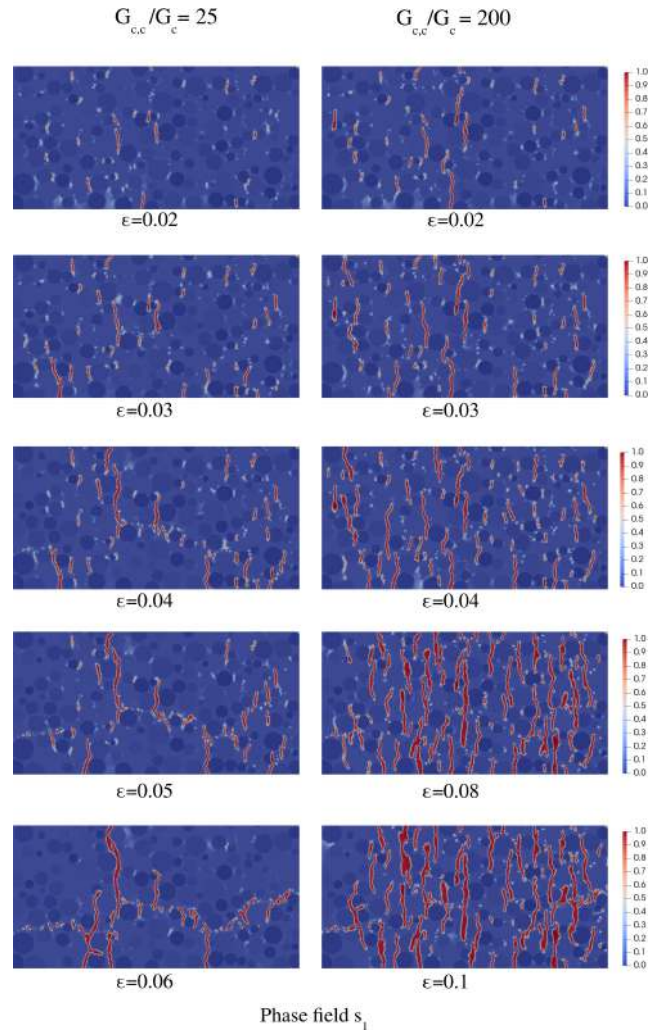


Figure 12: Contour plot of the phase field variable s_1 associated to fracture for the sample with $H/B = 0.5$ and low friction conditions, for different strain levels of increasing value from the top to the bottom. On the left the case with $G_{c,c}/G_c = 25$, while on the right the case with $G_{c,c}/G_c = 200$.

and compressive crushing occurring in quasi-brittle materials. Each dissipation mechanisms is ruled by its critical dissipated energy (fracture energy vs. crushing energy) and internal length scale.

The proposed variational approach has been applied to 2D mesoscale models of concrete specimens, considering typical material properties in tension and in compression available in the literature. For the sake of simplicity, and in absence of more accurate microscopical information, the internal length scales of the two failure mechanisms has been

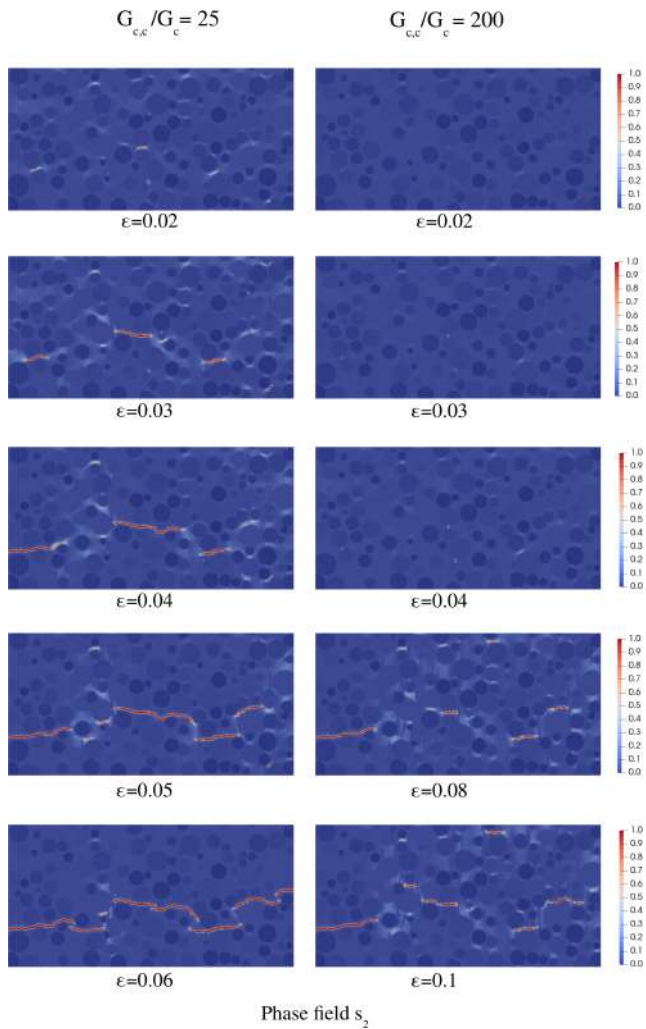


Figure 13: Contour plot of the phase field variable s_2 associated to crushing for the sample with $H/B = 0.5$ and low friction conditions, for different strain levels of increasing value from the top to the bottom. On the left the case with $G_{c,c}/G_c = 25$, while on the right the case with $G_{c,c}/G_c = 200$.

kept the same, although they can be treated as independent variables. Similarly, the same Poisson-type partial differential equation and the same form of the degradation function g has been kept for both failure mechanisms.

In spite of the above assumptions and the simulations restricted for now to 2D models, numerical predictions show an excellent ability to predict the well-known trends observed in the experiments. The simulated crack patterns of cylindrical and cubic specimens in compression are seemingly close to the experimentally observed ones. Cylindrical

specimens tend to fail in splitting, no matter of the degree of lateral constraint. On the other hand, the failure pattern of cubic specimens varies from splitting to shear band formation by increasing the level of lateral confinement. The effect upon the apparent strength is also quantitatively in line with experimental trends. Finally, Section 6 has highlighted the role of the crushing energy and the interplay with tensile fracture, which is properly captured by the computational method.

Once the present multi-phase field approach to tensile fracture and compressive crushing is established, further research is deemed to be essential for the fine tuning of the model parameters, especially the internal length scale associated to crushing. In that regard, in-situ compressive tests on quasi-brittle materials with digital microscopy observation of damage in the specimen might be crucial. Finally, it is worth mentioning that possible applications of the present model may concern not only quasi-brittle grained materials, but also porous materials as hard biological tissues.

Acknowledgements Support from the Italian Ministry of University and Research (MUR) to the Italian Project of National Interest PRIN 2017 XFAST-SIM 'Extra fast and accurate simulation of complex structural systems' (GA 20173C478N) is gratefully acknowledged.

References

- [1] G.A. Francfort, J.J. Marigo (1998) Revisiting brittle fracture as an energy minimization problem, *J. Mech. Phys. Solids* 46(8):1319–1342.
- [2] H. Amor, J.-J. Marigo, C. Maurini (2009) Regularized formulation of the variational brittle fracture with unilateral contact: numerical experiments. *J. Mech. Phys. Solids*, 57:1209–1229.
- [3] Z.P. Bažant, T.G.P. Pijaudier-Cabot (1988) Nonlocal continuum damage, localization instability and convergence, *J Appl. Mech.* 55:287–293.

- [4] M. Jirásek (1998) Nonlocal models for damage and fracture: Comparison of approaches, *Int. J. Solids Struct.* 35:4133–4145.
- [5] C. Comi, U. Perego (2001) Fracture energy based bi-dissipative damage model for concrete, *Int. J. Solids Struct.* 38:6427–6454.
- [6] D. Addessi, S. Marfia, E. Sacco (2002) A plastic nonlocal damage model, *Computer Methods in Applied Mechanics and Engineering* 191:1291–1310.
- [7] A.A Griffith (1921) The phenomena of rupture and flow in solids, *Philos. Trans. Royal Soc. Lond. A* 221:163–198.
- [8] Bourdin, B., Francfort, G.A., Marigo, J.-J. (2000) Numerical experiments in revisited brittle fracture. *J. Mech. Phys. Solids*, 48:797–826.
- [9] B. Bourdin, G.A. Francfort, J.J. Marigo (2008) The variational approach to fracture. *J. Elast.*, 91:5–148.
- [10] C. Miehe, M. Hofacker, F. Welschinger (2010) A phase field model for rateindependent crack propagation: robust algorithmic implementation based on operator splits, *Comput. Methods Appl. Mech. Engrg.* 199(45-48):2765–2778.
- [11] C. Miehe, F. Welschinger, M. Hofacker (2010) Thermodynamically consistent phasefield models of fracture: variational principles and multi-field FE-implementations, *Int. J. Numer. Methods Engrg.* 83(10):1273–1311.
- [12] I. S. Aranson, V. A. Kalatsky, V. M. Vinokur (2000) Continuum field description of crack propagation. *Phys. Rev. Lett.*, 85:118–121.
- [13] C. Kuhn, R. Müller (2008) A phase field model for fracture. *Proc. Appl. Math. Mech.*, 8: 10223–10224.
- [14] V. Hakim, A. Karma (2009) Laws of crack motion and phase-field models of fracture. *J. Mech. Phys. Solids*, 57:342–368.
- [15] C. Kuhn, R. Müller (2010) A continuum phase field model for fracture. *Eng Fract Mech*, 77:3625–3634.
- [16] T.T. Nguyen, J. Yvonnet, Q.-Z. Zhu, M. Bornert, C. Chateau (2015) A phase field method to simulate crack nucleation and propagation in strongly heterogeneous materials from direct imaging of their microstructure. *Engineering Fracture Mechanics*, 139:18–39.
- [17] M. Ambati, T. Gerasimov, L. De Lorenzis (2015) A review on phase-field models of brittle fracture and a new fast hybrid formulation. *Computational Mechanics*, 55:383-405.
- [18] M.A. Msekh, M. Sargado, M. Jamshidian, P. Areias, T. Rabczuk (2015) Abaqus implementation of phase-field model for brittle fracture. *Comput. Mater. Sci.* 96(B):472–484.
- [19] T. Gerasimov, L. De Lorenzis (2019) On penalization in variational phase-field models of brittle fracture. *Comput. Methods Appl. Mech. Engrg.*, 354: 990–1026.
- [20] D. Jodlbauer, U. Langer, W. Thomas (2020) Parallel Matrix-Free Higher-Order Finite Element Solvers for Phase-Field Fracture Problems. *Mathematical and Computational Applications*, 25(3).
- [21] J.Y. Wu (2017) A unified phase-field theory for the mechanics of damage and quasi-brittle failure. *Journal of Mechanics Physics of Solids*, 103:72-99.
- [22] J. Wambacq, J. Ulloa, G. Lombaert, S. Francois (2021) Interior-point methods for the phase-field approach to brittle and ductile fracture. *Comput. Methods Appl. Mech. Engrg.*, 375:113612.
- [23] E. Tanné, T. Li, B. Bourdin, J.-J. Marigo, C. Maurini (2018) Crack nucleation in variational phase-field models of brittle fracture. *Journal of the Mechanics and Physics of Solids*, 110:80–99.
- [24] F. Freddi, G. Royer-Carfagni (2010) Regularized variational theories of fracture: A unified approach. *Journal of the Mechanics and Physics of Solids*, 58: 1154–1174.
- [25] D.C. Jansen, S.P. Shah (1997) Effect of length on compressive strain softening of concrete, *J. Eng. Mech.* 123: 25–35.
- [26] K. Rokugo, W. Koyanagi (1992) Role of compressive fracture energy of concrete on the failure behaviour of reinforced concrete beams, *Applications of Fracture Mechanics to Reinforced Concrete* (A. Carpinteri, Ed.). Elsevier Applied Science, London: 437–464.
- [27] G. Ferrara, M.E. Gobbi (1995) Strain Softening of Concrete Under Compression. Report to RILEM Committee 148-SSC, ENEL-CRIS Laboratory, Milano, Italy.
- [28] A. Carpinteri, M. Corrado, M. Paggi, G. Mancini (2007) Cohesive versus overlapping crack model for a size effect analysis of RC elements in bending, *Proceedings of FraMCoS-6, Catania, Italy*, 655–663.
- [29] A. Carpinteri, M. Corrado, G. Mancini, M. Paggi (2009) The overlapping crack model for uniaxial and eccentric concrete compression tests, *Magazine of Concrete Research*, 61(9): 745–757.
- [30] A. Carpinteri, M. Corrado, M. paggi (2011) An analytical model based on strain localization .for the study of size-scale and slenderness effects in uniaxial compression tests, *Strain* 47:351–362.
- [31] A. Carpinteri, M. Corrado, M. Paggi (2010) An integrated cohesive/overlapping crack model for the analysis of flexural cracking and crushing in RC beams, *International journal of fracture*, 161(2):161–173.
- [32] A. Carpinteri, G. Lacidogna, N. Pugno (2004) Scaling of energy dissipation in crushing and fragmentation: a fractal and statistical

- analysis based on particle size distribution. *International Journal of Fracture*, 129(2): 131–139.
- [33] F. Indelicato, M. Paggi (2008) Specimen shape and the problem of contact in the assessment of concrete compressive strength, *Materials and Structures* 41:431–441.
- [34] A. Carpinteri, S. Puzzi (2008) Self-similarity in concrete fracture: size-scale effects and transition between different collapse mechanisms, *Int. J. Fract.* 154:167–175.
- [35] M.J. Borden, C.V. Verhoosel, M.A. Scott, T.J.R. Hughes, C.M. Landis (2012) A phase-field description of dynamic brittle fracture, *Comput. Methods Appl. Mech. Engrg.* 217–220:77–95.
- [36] Z.P. Bažant, H.T. Nguyen, A. Abdullah Dönmez (2022) Critical Comparison of Phase-Field, Peridynamics, and Crack Band Model M7 in Light of Gap Test and Classical Fracture Tests, *J. Appl. Mech.* 89(6): 061008.
- [37] J. Bleyer, R. Alessi, (2018) Phase-field modeling of anisotropic brittle fracture including several damage mechanisms, *Comput. Methods Appl. Mech. Engrg.* 336:213–236.
- [38] X. Xiong, Q. Xiao (2019) Meso-scale simulation of concrete based fracture and interaction behavior, *Appl. Sci.* 9:2986
- [39] T.T. Nguyen, J. Rethore, J. Yvonnet, M.C. Baietto (2017) Multi-phase-field modeling of anisotropic crack propagation for polycrystalline materials, *Comp. Mech.* 60(2):289–314.
- [40] A. Dean, P.K. Asur Vijaya Kumar, J. Reinoso, C. Gerendt, M. Paggi, E. Mahdi, R. Rolfes (2020) A multi phase-field fracture model for long fiber reinforced composites based on the Puck theory of failure *Composite Structures*, 251: 112446.
- [41] L. Ambrosio, V.M. Tortorelli (1990) Approximation of functional depending on jumps by elliptic functional via C-convergence, *Commun. Pure Appl. Math.* 43:999–1036.
- [42] L. Ambrosio, V.M. Tortorelli (1992) On the approximation of free discontinuity problems, *Boll. Un. Mat. Ital.* B(7)6(1):105–123.
- [43] H.P. Langtangen, A. Logg, A. Tveito (2016) Solving PDEs in Python: The FEniCS Tutorial I. Springer International Publishing.
- [44] A. Carpinteri, B. Chiaia, P. Cornetti (2003) On the mechanics of quasi-brittle materials with a fractal microstructure, *Engineering Fracture Mechanics*, 70:2321–2349.
- [45] G. Lilliu, J.G.M. van Mier (2003) 3D lattice type fracture model for concrete, *Engineering Fracture Mechanics*, 70:927-941.
- [46] T. Guillen Hernandez, I. García, J. Reinoso, M. Paggi (2019) A micromechanical analysis of inter-fiber failure in long reinforced composites based on the phase field approach of fracture combined with the cohesive zone model, *International Journal of Fracture*, 220, 181–203.